



Titan's bright spots: Multiband spectroscopic measurement of surface diversity and hazes

M. Ádámkóvics,¹ I. de Pater,¹ M. Hartung,² F. Eisenhauer,³ R. Genzel,^{3,4} and C. A. Griffith⁵

Received 18 October 2005; revised 20 February 2006; accepted 10 March 2006; published 21 June 2006.

[1] Spatially resolved near-infrared spectra of Titan, which simultaneously cover two CH₄ absorption bands (from 1.45 to 2.45 μm), have been obtained using the SINFONI integral-field spectrometer with adaptive optics at the Very Large Telescope (VLT) of the European Southern Observatory. We observe the enhancement in 2 μm surface albedo of the “5 μm bright spot” at 80°W and 24°S, and find an analogously bright region at 2 μm near 88°W and 6°S. Surface albedos are recovered at ~60 mas (375 km) resolution in both 1.5 and 2.0 μm windows using a two-stream, plane-parallel, radiative transfer model to fit the observed spectra. The surface albedos near the center of the disk range from 8 to 15% at 1.5 μm and are generally ~2% lower at 2.0 μm. Vertical (altitude) profiles of aerosol extinction that are consistent with the Huygens/DISR measurements are used to model these observations, and we retrieve latitudinal trends in both stratospheric and tropospheric aerosol extinction. On 28 February 2005 UT, the stratospheric aerosol extinction is measured to increase linearly at a rate of $0.65 \pm 0.05\%$ per degree latitude from 40°S to 60°N. Meanwhile, the tropospheric haze near the south pole is confined to southern latitudes above 40°S and is enhanced in extinction by a factor of ~1.7 relative to the extinction measured at 10°S, the latitude where the Huygens probe landed.

Citation: Ádámkóvics, M., I. de Pater, M. Hartung, F. Eisenhauer, R. Genzel, and A. Griffith (2006), Titan's bright spots: Multiband spectroscopic measurement of surface diversity and hazes, *J. Geophys. Res.*, *111*, E07S06, doi:10.1029/2005JE002610.

1. Introduction

[2] Saturn's moon Titan has a complex atmosphere with striking similarities to the supposed conditions of prebiotic Earth. The atmosphere is dense with N₂ (1.5 bar) and 94 K at the surface [Fulchignoni *et al.*, 2005]. The second most abundant gas, CH₄ (at 5% levels), is close to its triple-point [Kouvaris and Flasar, 1991] and takes part in a methane-based meteorological cycle that is similar to the Earth's hydrological cycle [Toon *et al.*, 1988; Tokano *et al.*, 2001; Lorenz and Rennó, 2002]. CH₄ is photolyzed in the upper stratosphere, which initiates a series of chemical reactions that result in the formation of condensable hydrocarbons and aerosols (at ~600 km). These aerosols settle throughout the atmosphere in numerous haze layers that change seasonally over global scales [Hutzell *et al.*, 1993, 1996]. Cassini spacecraft measurements have discovered that the hazes also

change on timescales as short as hours, although over smaller spatial scales [Porco *et al.*, 2005] (<http://ciclops.org/>). The dynamical redistribution of haze caused by aerosol formation, deposition, and transport occurs over a broad range of spatial and temporal scales.

[3] As the stratospheric aerosols settle into the troposphere, they can serve as condensation nuclei for Titan's methane and ethane clouds [McKay *et al.*, 2001]. Large clouds with lifetimes of several terrestrial weeks were first observed spectroscopically [Griffith *et al.*, 1998] and are now known to be localized near the southern pole [Brown *et al.*, 2002; Roe *et al.*, 2002b]. Another class of smaller clouds, with lifetimes of days, have been discovered near temperate regions [Roe *et al.*, 2005a]. The spatial distribution of these clouds seems to be localized in both latitude and longitude, indicating that their formation may relate to Titan's geography [Roe *et al.*, 2005b]. Indeed, mechanisms of cloud formation on Titan are now increasingly constrained by observations [Griffith *et al.*, 2005]. General circulation models (GCMs) that include cloud microphysics reproduce an assortment of cloud types with properties (such as location, lifetime and composition) that are determined by large-scale circulation [Rannou *et al.*, 2006]. Such models build the framework for understanding the dynamical and microphysical processes at work on Titan and would benefit from further observational constraints on clouds and aerosols.

[4] The seasonal variation in the global distribution of stratospheric haze was first observed using narrowband

¹Department of Astronomy, University of California, Berkeley, California, USA.

²European Southern Observatory, Santiago, Chile.

³Max-Planck-Institut für extraterrestrische Physik (MPE), Garching, Germany.

⁴Department of Physics, University of California, Berkeley, California, USA.

⁵Lunar and Planetary Laboratory, University of Arizona, Tucson, Arizona, USA.

filters on the Hubble Space Telescope (HST) at near-IR wavelengths ($0.89 \mu\text{m}$) [Caldwell *et al.*, 1992]. Narrowband imaging with HST was also used to measure the spatial and vertical distribution of tropospheric haze extinction [Young *et al.*, 2002], with the vertical (altitude) resolution apparently limited by the filter bandpass. Improved vertical resolution of haze extinction (as well as trace gas concentration and cloud altitude) could be obtained spectroscopically, however, until recently nearly all measured spectra of Titan were globally integrated. Spatial resolution was limited to imaging via spacecraft.

[5] Advances with ground-based adaptive optics (AO), which correct for the blurring caused by turbulence in Earth's atmosphere, have provided the opportunity to obtain spatially resolved spectra of Titan using conventional spectrometers. These techniques have been used to study clouds [Brown *et al.*, 2002] and haze [Ádámkovics *et al.*, 2004]. When considering spatial resolution and global coverage, such techniques are constrained by uncertainties in reconstructing the locations of the spectrometer slit, the slit width, and the total number steps across the observed disk, usually about 10, as limited by the total integration time. The spatial resolution obtained with this method limits analysis to relatively large features on the disk of Titan, larger than what can be resolved with narrow-band imaging.

[6] A more advanced approach uses integral-field spectroscopy [e.g., Hirtzig *et al.*, 2005] to measure the distribution of clouds, haze and surface albedo variation on Titan. Such techniques (often called integral-field spectroscopy, spectro-imaging, or mapping spectroscopy), yield a series of images (or datacubes) with 2 dimensions of spatial resolution and a third dimension of spectral resolution. Since observations at different near-IR wavelengths are sensitive to the haze extinction at various altitudes in Titan's atmosphere [Griffith and Owen, 1992], the three-dimensional distribution of aerosol haze can be retrieved using these spectral image datacubes. The benefits of integral-field spectroscopy over conventional spectrometers include a single PSF during the exposure (which facilitates the deconvolution of images), more reliable flux calibration, and decreased observation times. Acquiring spectra over the entire disk of Titan, in roughly the time it would take to acquire a single conventional spectrum, can reduce observing time by an order of magnitude. Integral-field spectroscopy thus facilitates higher signal-to-noise measurements across the target with improved spatial sampling (of the aerosol haze density or surface albedo, for example).

[7] In order to further constrain atmospheric models with quantitative retrievals of haze extinctions (so that the detailed coupling of photochemistry, microphysics and dynamics may be tested) we have used an integral-field spectrometer to retrieve the global distribution of aerosols on Titan. Although the basic features of Titan's haze during the Voyager era, such as the southern polar enhancement and the detached haze layer, have been reproduced with GCMs that couple photochemistry and aerosol microphysics [Hourdin *et al.*, 1995; Rannou *et al.*, 2002, 2004], these models made assumptions about the tropospheric and lower stratospheric aerosols (such as size, shape, and density) that could not be constrained with observations. Subsequent observations of subtle and seasonal variations were not predicted by models. For example, Cassini observations in

2005 found the detached haze to be higher and thinner than during the Voyager era, as well as a series of thin stratified haze layers [Porco *et al.*, 2005]. We report here the first adaptive optics measurements of Titan using the SINFONI integral-field spectrograph on the Very Large Telescope (VLT) along with an efficient method for haze extinction and surface albedo retrieval using a two-stream, plane-parallel, radiative transfer model. We measure the global variation in tropospheric and stratospheric haze extinction as well as the surface albedos in both H- and K-bands.

2. Observing With SINFONI

[8] Since April 2005 (ESO period 75) the new adaptive optics (AO) assisted integral-field spectrometer SINFONI has been available to the astronomical community [Eisenhauer *et al.*, 2003a; Bonnet *et al.*, 2004]. The instrument is mounted at the Cassegrain focus of the Very Large Telescope (VLT) Unit Telescope 4 (Yepun). SINFONI consists of a cryogenic integral-field spectrometer with a $2\text{K} \times 2\text{K}$ Hawaii detector (SPIFFI [Eisenhauer *et al.*, 2003a, 2003b]), coupled to a curvature sensor AO unit (MACAO [Bonnet *et al.*, 2003]). The spectrometer uses two sets of 32 stacked mirrors to slice the field of view into 32 "slitlets," which are then rearranged to a form a "pseudo long slit" that is dispersed onto the detector. Each of the 32 "slitlets" is imaged onto 64×2000 pixels.

[9] Our SINFONI Titan observations were conducted during final commissioning runs on 28 February 2005 from UT 03:05 to 03:52 at 1.6 to 1.8 airmasses. The 60 actuator MACAO AO system was locked on Titan under favorable atmospheric conditions. The night was photometric, the seeing stayed stable around $0.6''$, and the coherence time varied between 4 and 6 msec, ensuring optimal performance of the AO module and imaging close to the diffraction limit of the VLT (60 mas in K-band).

[10] We employed the highest spatial resolution mode with $0.0125'' \times 0.025''$ (EW \times NS) pixels fully covering a contiguous field of view of $0.8'' \times 0.8''$, matching almost ideally the diameter of Titan ($0.85''$ at the time of observation). We applied the H+K grating, which simultaneously delivers a spectrum (for each spatial pixel) across the entire $1.45 - 2.45 \mu\text{m}$ region at resolving power, $R \sim 2000 - 3400$, where $R = \lambda/\Delta\lambda$. The spectral pixels have a $\Delta\lambda$ (FWHM) of $7 - 8 \times 10^{-4} \mu\text{m}$. In order to cover the full disk of Titan and to allow for bad pixel correction, we acquired 8 object-sky pairs of 120 sec integration time each, spatially dithered over a squared region of $1.1''$ centered on the observed disk of Titan at an effective spatial pixel sampling of 12.5 mas.

[11] The OH airglow was eliminated by subtraction of the sky cubes. After flat-fielding, wavelength calibration, and dead/hot pixel interpolation, the final data cubes were divided by the spectrum of an G2V star (Hip040798) to compensate for telluric absorption. The spectrum of a telluric standard star was taken 1 hr after the Titan observation at 1.3 airmasses, which violates slightly the conventional constraint of 0.1 airmass difference in respect to the science target. Finally, the cube was multiplied by a solar spectrum (to correct for the G2V telluric standard) convolved with the instrumental spectral profile and Doppler-shifted to match the radial velocity of the star. Conversion to units of geometric albedo, I/F , was performed using the absolute solar flux spectrum of Colina *et al.* [1996].

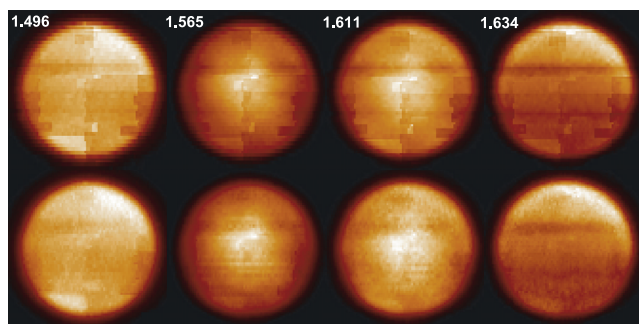


Figure 1. The mosaicked images from the VLT reduction pipeline have prominent artifacts that form a relatively fixed pattern across a broad (~ 250 nm) wavelength range in both H- (top) and K-bands (not shown). To account for these artifacts, correction masks are generated via a low-pass filter at each sampled wavelength (see text). The set of masks are collapsed to form single correction mask by median filtering over 20 nm in wavelength, and this mask is used to correct each of the images (bottom). Celestial north is up, and east is to the left.

[12] The wavelength calibration was done using arc-lamp spectra recorded during the day, and the fine-tuning of the zero-wavelength was performed with the help of the night-sky emission lines. The accuracy of wavelength calibration is expected to be better than 0.1 nm. The atmospheric dispersion was corrected for individual datacubes before mosaicking the data together. At 1.6 to 1.8 airmasses the dispersion is not negligible. However, after the dispersion correction, the effect is reduced to less than 1 spatial pixel.

[13] A significant artifact of observing a bright extended object is a so-called “memory effect” on the detector, which results in what appears to be an inadequate flat-fielding. We corrected for this by generating a correction mask that takes advantage of the weak wavelength dependence of this artifact. To make a mask, the image at each wavelength was low-pass filtered by convolution with 3×3 pixel mean value kernel, essentially box-car smoothing. Then, the filtered image was rotated from -10° to $+10^\circ$ in 1° steps, and the ratios of the filtered images to the original were averaged to generate a mean correction mask. After an averaged mask was calculated at each wavelength, we median filtered the masks over a 20 nm window to correct each image (Figure 1). Artifacts that span a large fraction of the disk, such as the dark stripe in top half of the disk, are not completely removed because we used a small convolution kernel. Removing such large artifacts would require smoothing over regions larger than the spatial resolution of the instrument and would therefore smear out the observed contrast of real features. In order to improve the raw data, an improved observational protocol could involve increasing the number of object-sky pairs that are dithered across the disk of Titan, or a better characterization of the detector response to bright extended objects could be incorporated into the reduction pipeline.

3. Model-Independent Results

[14] A small fraction of the large data set that was obtained with SINFONI is presented in Figure 2. These 32 images are each integrated over 5 nm bandwidth and

account for roughly 1/8th of the entire data set. The three general regions of Titan’s atmosphere that are probed at these wavelengths are the surface, the troposphere (0 – 40 km) and the lower stratosphere (40 – 200 km). Inspection of images in Figure 2, at wavelengths that probe the stratosphere, indicates that there is more haze in the northern hemisphere while at the wavelengths that probe the troposphere there is more haze near the south pole. This is modeled quantitatively and described in detail in sections 4.5 and 4.6.

[15] The viewing geometry on 28 February 2005 UT was such that a “bright” continent (so-called “Xanadu”) was in the center of the disk surrounded by darker regions. On this fraction of the globe there is less surface albedo contrast than, for example, at 20°S and 110°W . At first glance it may seem that the spatial-resolution of these images is not superlative. Comparing the intensity contrast in the VLT/SINFONI images (at the wavelengths that probe surface albedo variations) with a reprojection of the $0.938 \mu\text{m}$ Cassini Imaging Science Subsystem (ISS) map [Porco *et al.*, 2005] illustrates the exceptional spatial resolution achieved from the ground with the SINFONI imaging spectrograph (Figure 3).

[16] These data are the first ground-based measurements of Titan with both spatial resolution and the simultaneous acquisition of multiple near-IR bands. With these data we can make a direct comparison of H- and K-band surface albedo contrasts retrieved at spectral resolutions above $R \sim 2,000$ (discussed in section 4.7). It can be seen in Figure 3 that the brightest regions in H-band do not correspond to the brightest regions in K-band. Not surprisingly, the “5 μm bright spot” (5 μmBS) reported by Barnes *et al.* [2005] at 80°W and 25°S is also observed here to be exceptionally bright in K-band. We also report another particularly bright spot in K-band, northwest of the original 5 μmBS , at 88°W and 6°S . This second spot is also observed in the 2003 Keck K-band image of Barnes *et al.* [2005]. It seems that this location may only be observable in 2 of the 5 Cassini/VIMS fly-by images (TA and TB) presented by Barnes *et al.* [2005], so it is unclear if this second spot is also bright at 5 μm . Yet there does seem to be another 5 μmBS at roughly the same location as the bright K-band spot in the TA and TB images, suggesting that the original 5 μmBS is not unique. It is noteworthy that these two spots are both located on the particularly bright continent, Xanadu. Similar prominent spots have not been observed in K-band images of other regions on Titan (see, for example, the Keck Titan monitoring project: <http://www2.keck.hawaii.edu/science/titan/>), and one cannot rule out a link between the brightness of these two features and the overall brightness of the continent.

[17] Spectra of these two bright regions indicate that the increased 2 μm intensity likely arises from the surface. When compared with three neighboring regions, the K-band spectra of the two bright spots diverge at wavelengths below 2.1 μm (Figure 4), where less than 1% of the intensity comes from the boundary layer (below 1 km). The observed K-band I/F is $\sim 0.5\%$ larger on the bright spots than the surrounding regions on the continent, however this is a lower limit to the increase in the albedo because the spots are unresolved. Indeed, measurements conducted with Cassini/VIMS indicate that the 5 μmBS is $\sim 2\%$ brighter in K-band than surrounding regions on Xanadu. Somewhat less

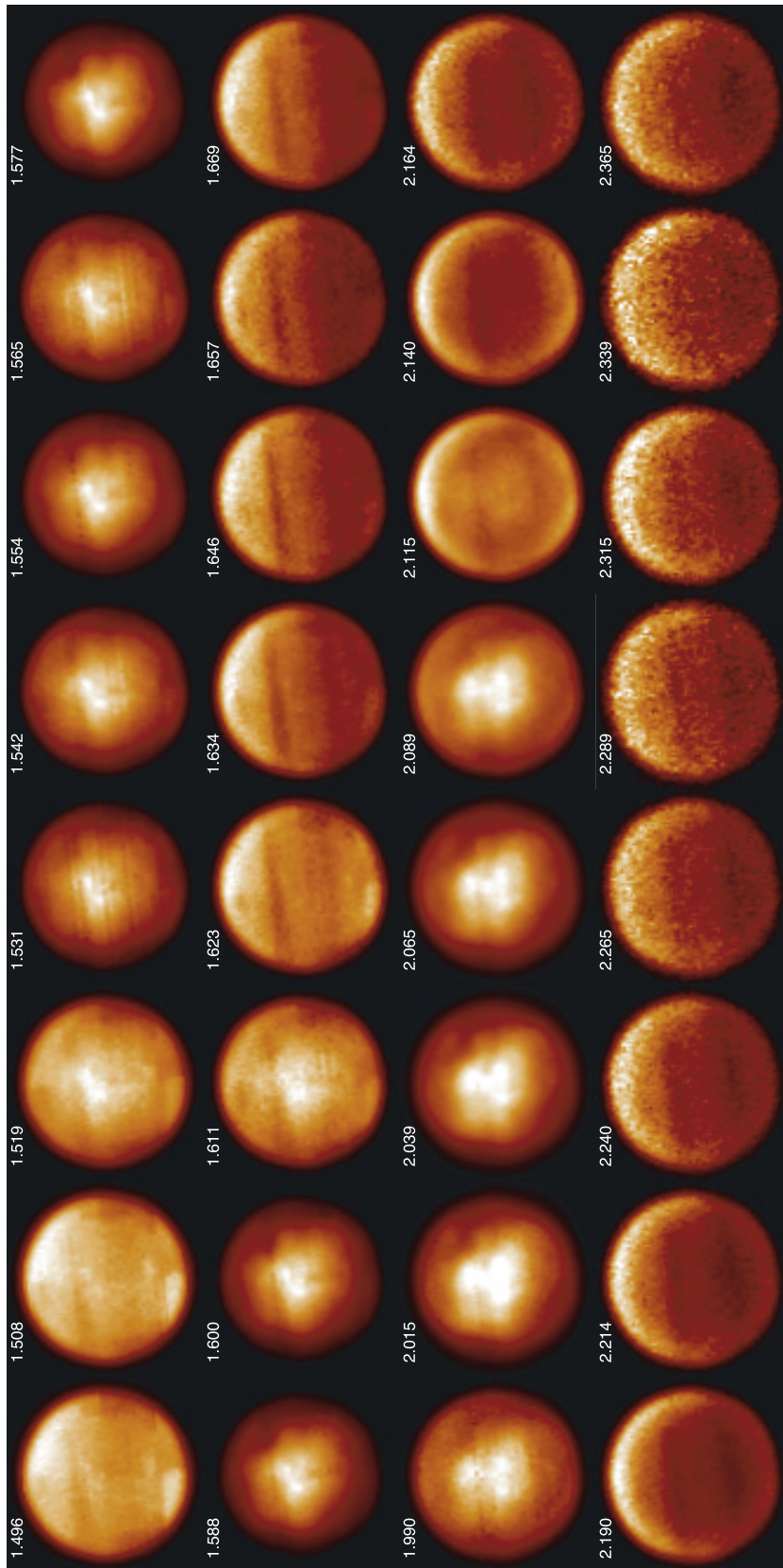


Figure 2. Characteristic images of Titan in both H-band (1.4 – 1.8 μm) and K-band (1.9 – 2.5 μm) observed using VLT/SINFONI. Central wavelengths (in μm) are shown to the upper left of each image, and the bandwidth is 5 nm. Images are rotated so that Titan north is up with the subobserver point at -23.4°S and 89.5°W (west longitude increasing to the left). The observed intensity is stretched linearly between 30 and 100% of the maximum intensity in each image. Both H- and K-band windows contain wavelengths that probe the surface (e.g., 1.588 and 2.039 μm), the troposphere (e.g., 1.611 and 2.140 μm), and the stratosphere (e.g., 1.669 and 2.190 μm). At these wavelengths, increased intensity is due to increased aerosol extinction, so the stratospheric haze has a higher concentration near the north (winter) pole, and the tropospheric haze is enhanced near the south pole, which is most clearly observed in the 2.140 μm image. At 2.140 μm there is also a contribution to the observed intensity from the stratospheric haze near the north pole.

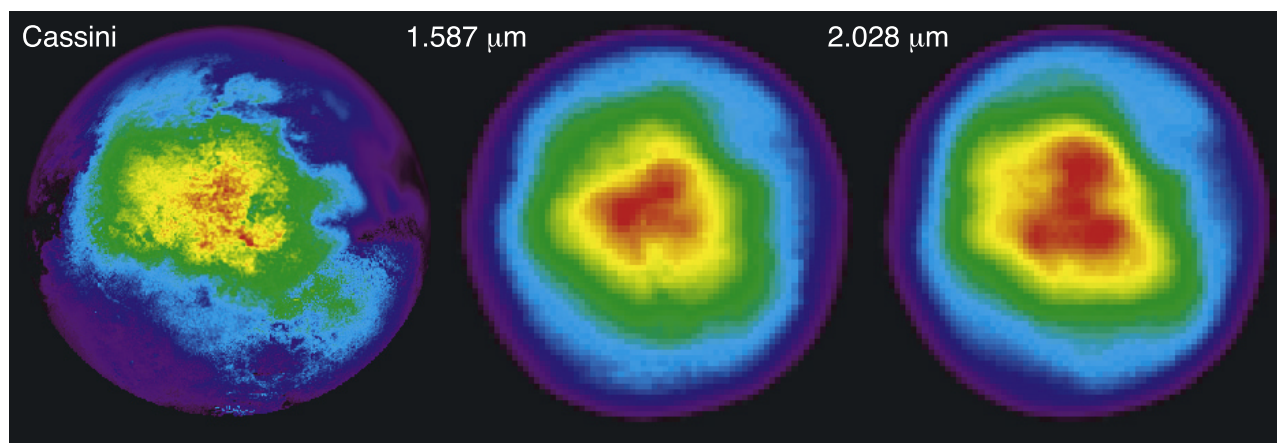


Figure 3. Comparison of VLT/SINFONI observations in both H- and K-bands with a reprojection of the $0.938\ \mu\text{m}$ Cassini surface intensity map [Porco *et al.*, 2005] at subobserver point -23.4°S and 89.5°W . The $5\ \mu\text{mBS}$ reported by Barnes *et al.* [2005] is located at the bright semicircular “smile” feature in the Cassini image that is just to the right of disk center, and corresponds with the bright feature in the $2.028\ \mu\text{m}$ VLT image. The 1.587 and $2.028\ \mu\text{m}$ VLT images are linearly stretched between I/F of $0.06 - 0.185$ and $0.04 - 0.132$, respectively. The Cassini map intensity is an arbitrarily scaled linear intensity map with a limb darkening function of the form $f(r) = \cos(\pi r/2R_T)^k$, where r is the distance from disk center, R_T is Titan’s radius, and $k = 0.7$. Surface albedo calculations are discussed in section 4.7 and shown in Figure 12.

speculative analysis can be aided by a spectroscopic measurement of the surface albedo in these regions. To do this, the atmosphere must first be modeled.

4. Haze Extinction and Surface Albedo Retrieval

[18] All of Titan’s observed near-IR intensity is sunlight scattered by aerosols or reflected from the surface. The size,

structure, and chemical composition of an aerosol will determine how the particle scatters light, and the measurable details of the scattering (the phase function, polarization, and amount of absorption) will be wavelength dependent quantities. Any remote observation will measure scattering from a large number of particles with a distribution of sizes, structures, and compositions, each of which depend on the altitude and location of the particular ensemble of particles

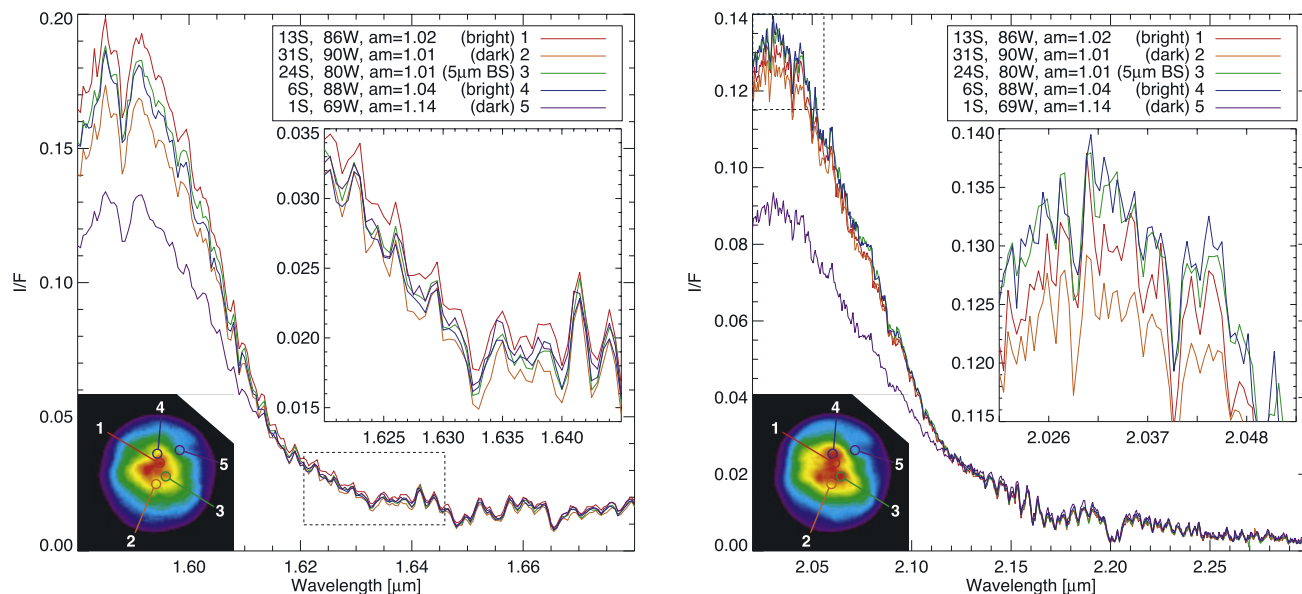


Figure 4. The observed spectra from 5 locations on the disk (in both H- and K-bands) that correspond to (1) a bright surface region on the continent in H-band near disk center, red, (2) a relatively dark surface region on the continent in H-band, orange, (3) the $5\ \mu\text{mBS}$ region, green, (4) another very bright region in K-band, blue, and (5) a particularly dark region at the edge of the continent, purple. The inset images (from Figure 3) show the locations of the spectra. The H-band inset illustrates the general latitudinal dependence of the spectra at wavelengths probing the stratosphere, while the K-band inset highlights variations at wavelengths that probe the surface.

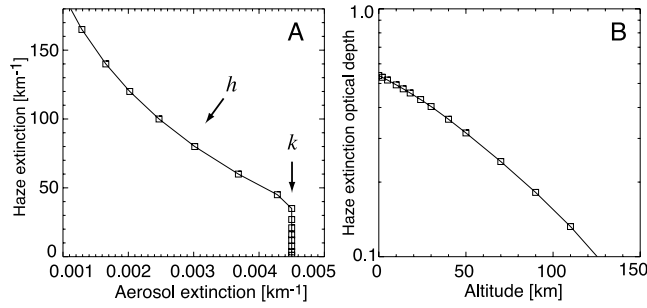


Figure 5. The vertical profile of the haze extinction near the subobserver point plotted as (a) extinction per modeled atmospheric layer and (b) as cumulative extinction optical depth for comparison with the Huygens/DISR extinction profile. By assuming a fixed stratospheric extinction scale height, $h = 100$ km, and a constant tropospheric extinction, the entire profile can be defined by the extinction at the surface, which we call the extinction parameter, k .

being probed. On Titan, some combination of these properties change with time and result in seasonal changes in Titan's albedo [Lorenz *et al.*, 2001]. These changes in albedo are commonly interpreted as changes in the aerosol density, primarily driven by circulation [Rannou *et al.*, 2002].

[19] As the Huygens probe descended onto Titan's surface, the DISR instrument provided the most comprehensive and detailed constraints on the vertical distribution of aerosols and how they scatter light [Tomasko *et al.*, 2005]. We use an aerosol extinction profile (described in Figure 5 and Table 1) that matches the one measured by DISR at $1.5 \mu\text{m}$ to constrain and validate the parameterization of the aerosol scattering in our radiative transfer calculations. Global variation in the observed albedo is discussed in terms of changes to this characteristic vertical profile.

4.1. Radiative Transfer and Opacities

[20] The radiative transfer methodology presented here has been regularly used to study the near-IR haze and cloud opacity on Titan [Griffith *et al.*, 1991; Brown *et al.*, 2002; Adámkovics *et al.*, 2004]. Briefly, a 2-stream approximation solves the radiative transfer equation for 16 plane-parallel layers from 0 to 200 km altitude [Toon *et al.*, 1989; McKay *et al.*, 1989]. We use the atmospheric temperature and profiles measured in situ by Huygens/HASI [Fulchignoni *et al.*, 2005], which are in excellent agreement with Voyager profiles [Lellouch *et al.*, 1989] below 200 km.

[21] Aerosol scattering is treated with a single parameter Henyey-Greenstein phase function using a constant single-scattering albedo, $a = 0.95$, that is consistent with laboratory measurements of the complex index of refraction for haze analog particles [Khare *et al.*, 1984]. When modeling these observations the same observed intensity can be reproduced with a greater/lower extinction if the aerosols are more forward/backward scattering. It has been general practice to argue for some scattering phase function (for example, via Mie theory at a given particle size) and then vary the extinction to match the observations. Here we use the $1.5 \mu\text{m}$ Huygens/DISR profile with our observed spectra

from near the latitude of the Huygens landing site, 10°S , to constrain the phase function parameter, g .

[22] The dominant gas-phase sources of opacity in these wavelength regions are the $2\nu_3$ band [Rank *et al.*, 1961; Margolis, 1988] and $\nu_2 + \nu_3$ band [Hilico *et al.*, 1992] absorptions of CH_4 . The vertical profile of CH_4 mole fraction (or mixing ratio) is defined to match the measurements made by Huygens/GCMS [Niemann *et al.*, 2005]. We use the absorption coefficients for CH_4 presented by Irwin *et al.* [2006] to calculate CH_4 opacities. Near the band centers at $1.65 \mu\text{m}$ and $2.20 \mu\text{m}$, where CH_4 absorption is strongest, the observed sunlight is reflected high in the stratosphere from aerosol haze [Griffith *et al.*, 1991]. On the edges of the CH_4 bands absorption is weak and the surface albedo variations are measured. Intermediate wavelengths probe correspondingly intermediate altitudes in the atmosphere.

[23] Other sources of gas-phase opacity in the K-band include low-temperature collision-induced absorption by N_2 and H_2 [McKellar, 1989]. The $\text{H}_2\text{-N}_2$ collision complex is a significant source of opacity near $2.1 \mu\text{m}$ that decreases the observed slope of Titan's spectrum in K-band relative to H-band (Figure 4). Since the observed I/F maps roughly onto the altitude where most of the observed intensity originates, the gradual variation in K-band extinction facilitates altitude discrimination relative to H-band.

4.2. Contribution Functions

[24] To demonstrate the mapping of a particular wavelength, λ , to the altitude region of Titan's atmosphere that is probed, we calculate the contribution function, $C_\lambda(n)$, with our two-stream model. The upward fluxes, F_n^u and F_n^d , are determined in the model at the upper and lower boundaries, respectively, of each atmospheric layer, n . The fraction of

Table 1. Characteristic Haze Extinction and Optical Depths That Match the Huygens/DISR Extinction Profile at $1.5 \mu\text{m}$ ^a

Alt, ^b km	Extinction, km^{-1}	Layer Optical Depth	Optical Depth ^c
180	0.0010	0.020	0.020
150	0.0013	0.039	0.059
130	0.0017	0.033	0.092
110	0.0020	0.040	0.132
90	0.0025	0.049	0.182
70	0.0030	0.060	0.242
50	0.0037	0.074	0.316
40	0.0043	0.043	0.359
30	0.0045	0.045	0.404
24	0.0045	0.027	0.431
18	0.0045	0.027	0.458
14	0.0045	0.018	0.476
10	0.0045	0.018	0.494
5	0.0045	0.022	0.516
2	0.0045	0.013	0.530
0	0.0045	0.009	0.539
	τ_{trop}	0.180	
	τ_{strat}	0.359	

^aThe tabulated values are calculated using a haze extinction parameter, $k = 0.0045 \text{ km}^{-1}$. Extinction is constant at this value up to 40 km, above which extinction decreases with a scale height, $h = 100$ km. τ_{trop} and τ_{strat} are the haze extinction optical depths for the troposphere and stratosphere, respectively.

^bAltitude at bottom of atmospheric layer.

^cOptical depth at bottom of atmospheric layer.

photons at the top of the atmosphere that arise from a particular layer can be calculated numerically using

$$C_{\lambda}(n) = \left[F_n^u - F_n^l e^{-\tau_n/\mu_n} \right] \times \exp \left(- \sum_{i=n+1}^N \tau_i/\mu_i \right) / F_0$$

where F_0 is the observed flux from the top of the atmosphere and τ_n is the optical depth of layer n scaled by the pathlength through the layer, $1/\mu_n$. The pathlength is determined by the effective incidence angle, μ (described below). The terms in the brackets are the difference in upward fluxes, which take into account the optical depth of the layer. The summation accounts for attenuation of the upward flux by the total optical depth above the atmospheric layer being considered, up to the topmost layer, N . The flux is normalized relative to the observed flux, F_0 . The layers in the model are not uniform in thickness (Table 1), and thicker layers will have larger contributions to the observed flux. To compare the contribution at different altitudes, we normalize the contribution $C_{\lambda}(n)$ by the layer thickness, δz , in km. Normalized contribution functions have been calculated for individual wavelengths from 1.61 to 1.65 μm and from 2.01 to 2.17 μm . Figure 6 illustrates that longer wavelengths (in this spectral region) probe higher altitudes in the atmosphere. We show the contributions for an atmosphere with an extinction profile that matches the 1.5 μm Huygens/DISR profile and a phase function that best fits observed spectra at 10°S latitude.

4.3. Geometric Limb Correction

[25] In the plane-parallel approximation of a spherical atmosphere, path lengths are overestimated at large incident angles and cause exaggerated limb brightening and darkening. This is a good approximation if the size of the atmosphere is small compared to the radius of the target. For Titan, however, the extent of the atmosphere above the surface that we consider (up to 200 km) is a sizable fraction of the total radius (2575 km). Modeling the limb of Titan with plane-parallel approximations can be improved by using a variable path through the atmosphere [Samuelson and Mayo, 2001]. Here we correct the plane-parallel approximation by calculating an effective incident angle, θ , at the bottom of each atmospheric layer. The geometrical correction factor (as described by Tran and Rannou [2004]) is of the form

$$\mu = \left[1 - \left(\frac{R}{R+z} \right)^2 + (1 - \mu_0^2) \right]^{1/2}$$

where R is the radius of the planet, z is the altitude at the bottom of the atmospheric layer, and $\mu_0 = \cos\theta_0$. θ_0 is the incident angle at the surface and we use the typical notation, $\mu = \cos\theta$. Tran and Rannou [2004] have validated this correction for Titan with three-dimensional spherical Monte Carlo calculations.

4.4. Fitting the Observed Spectra

[26] By using the aerosol extinction profile measured by Huygens/DISR and the CH_4 mixing ratio measured by the

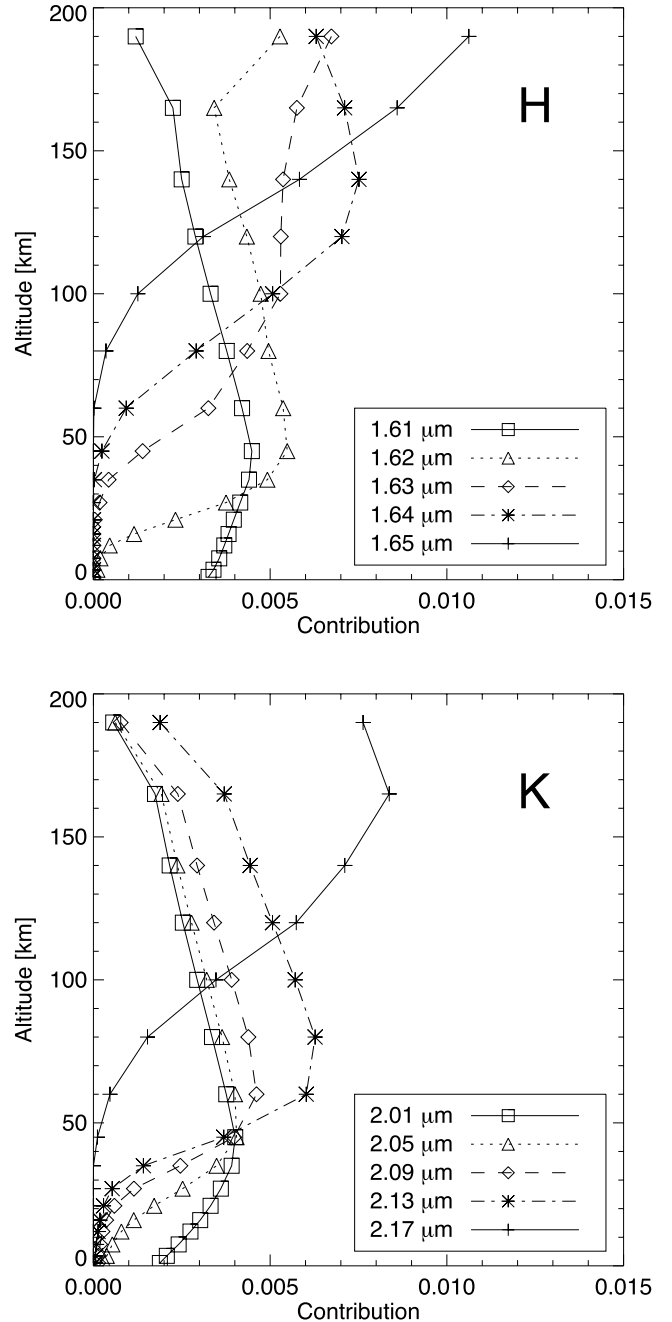


Figure 6. Normalized contribution functions for various wavelengths in H-band (H) and K-band (K), calculated by using the upward fluxes, F_n^u and F_n^l , at the boundaries of each atmospheric layer.

Huygens/GCMS, we need only two free parameters (the surface albedo, a_{surf} , and the phase function, parameterized by g) to fit a spectrum of Titan observed near the time of probe entry and near latitude of the landing site. After the phase function has been determined here, it is held fixed and the extinction is varied to model spectra from other regions on the disk. We use the 5 spectra in Figure 4 to demonstrate the radiative transfer modeling. To begin the procedure, a series of spectra are calculated by varying g in steps of 0.01. The phase function is wavelength dependent so we specify

g_H and g_K for H- and K-bands, respectively, and fit them independently. For a given location, each of the calculated spectra are compared against the observed spectrum by calculating the mean squared deviation, χ , from 1.64 to 1.70 μm in H-band or from 2.15 to 2.25 μm in K-band. This determines the best scattering phase functions, $g_H = 0.47 \pm 0.02$ and $g_K = 0.67 \pm 0.01$. These are moderately forward scattering phase functions that differ from the strongly forward scattering phase functions that have long been used to fit the Voyager 2 [West *et al.*, 1983] and Huygens measurements [Tomasko *et al.*, 2005]. We do not argue here that these observations suggest a different scattering phase function for Titan's aerosols. Rather, these values for g_H and g_K are the best approximation of the phase function to use with our two-stream approximation and the Huygens/DISR extinction profile. Since the measurements presented here are most sensitive to the backscattering component of the phase function (due to the small phase-angle (4.7°) of the observations), the 1-term parameterization underpredicts the forward-scattering. Large phase angle and in situ observations are better ways to measure the scattering phase function of Titan's aerosol.

[27] Once g has been determined the surface albedos in the two bands are varied to match the spectra below 1.60 and 2.05 μm . We model a surface albedo that is independent of wavelength within each band. The observations are compared with calculated spectra in Figure 7. The surface albedos in H-band are in the 8.5 – 14.7% range, which are in agreement with the $\sim 8\%$ surface reflectivity reported by Tomasko *et al.* [2005]. The regions probed by these 5 spectra are some of the brightest terrain in the Cassini/ISS maps of Titan [Porco *et al.*, 2005], so we expect to measure slightly higher surface albedos than at the Huygens landing site.

[28] To retrieve the H-band surface albedo the goodness of fit is determined by minimizing χ over the wavelength range 1.590 – 1.592 μm . By matching the intensity in this wavelength range, where the observed spectra peak, we presume that our radiative transfer model underestimates the gas phase opacity as well as any resolved absorption features on the surface. Comparing the observations with the calculations in Figure 7 indicates that this is indeed the case. The calculated spectra below 1.62 μm rise more steeply than the observations and the CH_4 opacity at 1.565 μm is drastically underestimated. When the observations are fit in the 2.05 – 2.15 μm range, the K-band spectra also show an underestimate of the gas opacity below 2.05 μm . By comparing the peak values in the observations and the calculated spectra, the K-band a_{surf} is overestimated by $\sim 2\%$.

[29] We interpret the discrepancy between the observed and the modeled spectra as an underestimate of CH_4 opacity by Irwin *et al.* [2006] for regions of weak CH_4 transitions. However, there may be additional sources of gas-phase opacity in these regions that have yet to be identified and absorption features on the surface [Griffith *et al.*, 2003]. The HITRAN 2004 database has $\sim 1,000$ CH_4 transitions in the 1.573 – 1.638 μm [Rothman *et al.*, 2005]. Although it is tempting to consider a line-by-line calculation of the CH_4 absorption coefficients at these wavelengths, none of these transitions are assigned. The intensity of the transitions is only known at 298 K and not at the temperatures (below 200 K) that are relevant for Titan. Currently, the CH_4

absorption coefficients reported by Irwin *et al.* [2006] are the best available for Titan.

4.5. Stratospheric Haze

[30] In order to quantify the observed global variation of stratospheric haze (e.g., at 1.669 μm in Figure 2), we determined the best H-band extinction parameter, k_H , for each of observed spectra. Spectra were fit in the 1.64 – 1.70 μm region by varying the extinction parameter, k , while using a fixed scattering phase function, $g_H = 0.47$. After retrieving k_H at each point on the disk, we noted that there was a radial dependence to the observed stratospheric extinction (Figure 8, inset A). Values of k_H are smaller near the limb, which is consistent with an overestimate of the pathlength there. Although we corrected for the pathlength near the limb in plane-plane approximation (section 4.3), this was not sufficient for reproducing the observed spectra. Even with the geometric correction the uncertainties in both the haze extinction profile and the two-stream approximation are greater near the limb.

[31] We can compensate for the artificial radial dependence of the retrieved k_H by assuming that there should be no longitudinal variation in the haze at a given latitude and empirically correcting our observations. To do this we take 3 strips (Figure 8, inset B) of retrieved k_H values at constant latitude and plot them as a function of the distance, R , from the center of the disk (Figure 8). The observed k_H are fit to a two-term polynomial, with the best fit of $k_H(R) = 1 + 0.081R - 0.640R^2$. This function is used to correct for the radial dependence of each the retrieved values of k_H . After this correction the values of k_H show only a latitudinal dependence (Figure 8, inset C).

[32] The same procedure can be done in K-band, where k_K is fit in the 2.15 – 2.25 μm region, using $g_K = 0.66$. The radial dependence has consistent fit coefficients and the latitudinal dependence of the stratospheric haze matches the trend in H-band.

[33] The latitudinal dependence of the stratospheric haze can be illustrated by plotting a north-south strip of corrected k_H as a function of latitude (Figure 9). The stratospheric haze is constant at southern latitudes above 40°S , and increases linearly to the north at a rate of $0.65 \pm 0.05\%$ per degree latitude from 40°S to 60°N . Without the empirical correction to the radial dependence of the retrieved k_H , which is only possible with longitudinal resolution, the retrieved stratospheric extinction would peak near the equator and decrease toward each pole, which is contrary to both a qualitative interpretation of the raw data (Figure 2) and models of Titan's circulation [Rannou *et al.*, 2002].

4.6. Tropospheric Haze

[34] The tropospheric haze is known to be decoupled from the stratosphere; that is, a single vertical profile cannot be scaled linearly at all altitudes and reproduce the observations from various locations on Titan. For example, the stratosphere can be enhanced in aerosol density in the northern hemisphere, while the troposphere is enhanced in aerosol density in the southern hemisphere [Roe *et al.*, 2002a]. While it had been the convention in modeling the near-IR spectra of Titan to assume a clearing of tropospheric aerosol below some altitude [e.g., Toon *et al.*, 1992; Young *et al.*, 2002; Ádámkovics *et al.*, 2004], the Huygens obser-

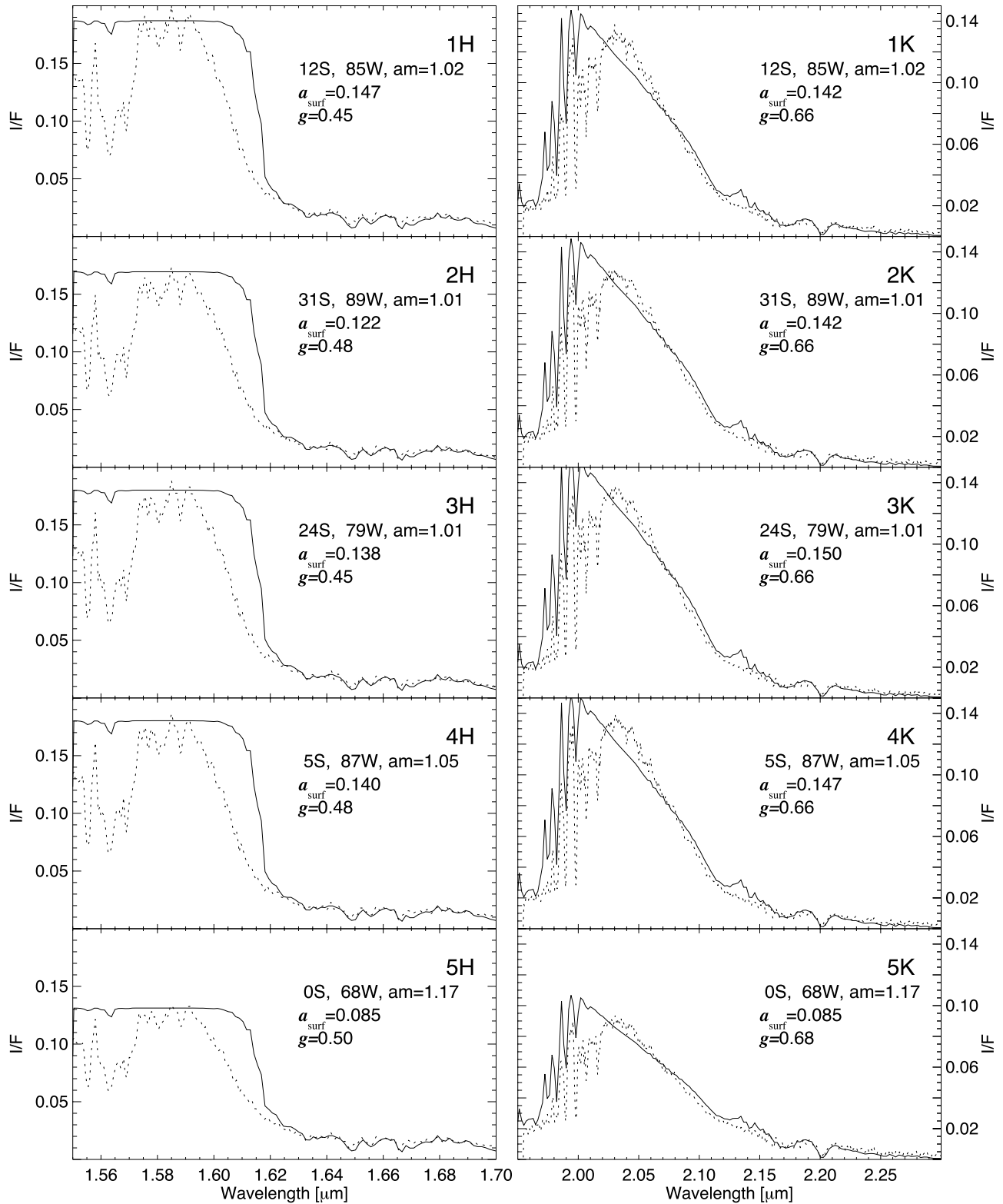


Figure 7. The five observed spectra from Figure 4 are shown here with the best fit model. The latitude, longitude, airmass on Titan (am), best fit surface albedo (a_{surf}), and best fit 1-term Henyey-Greenstein phase function parameter (g) are given for each spectrum. The regions of low I/F that probe the stratosphere (where there is deep, well-characterized CH_4 absorption) are well fit, whereas the fits of the spectra at wavelengths that probe the surface are poor, perhaps due to an underestimate of the gas opacity.

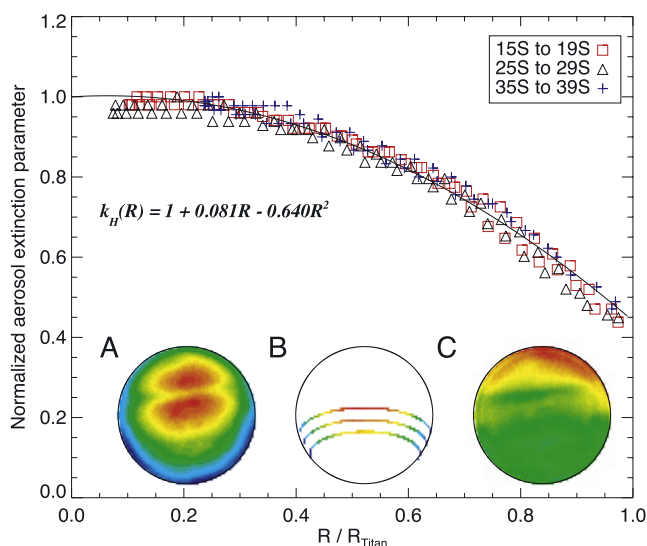


Figure 8. The radial dependence of the retrieved H-band extinction parameter, k_H , is illustrated by plotting k_H in three latitude bands. Here k_H has been fit to the observations in a wavelength region that is sensitive to stratospheric extinction. Inset A is an image of the value of k_H at each location on the disk, with the “memory effect” from the mosaicking still noticeable as a stripe. Inset B shows the locations of the values of k_H in 3 latitude bands, which are plotted in the figure; a second-order polynomial is fit to these points, with the two fit coefficients given in the functional form for $k_H(R)$. Inset C shows the same data as inset A after correction with the best fit polynomial.

vations have shown that this is incorrect [Tomasko *et al.*, 2005], and instead Titan’s troposphere has a roughly constant aerosol extinction. With hindsight it can be argued that the altitude at which the clearing was assumed to occur provided a parameter to adjust the total tropospheric haze opacity. However a constant vertical distribution of this tropospheric opacity was never considered because it was not predicted by microphysical models.

[35] We model the enhancement (or depletion) in tropospheric opacity, relative to the Huygens/DISR profile by linearly scaling the haze extinction in the troposphere (from 0 to 40 km) while keeping the best fit stratospheric extinction. As described in section 4.1, the K-band has better altitude discrimination than H-band. Figure 10 shows the value of tropospheric enhancement (relative to the best fit stratospheric value) that produces an optimal fit to the observations. Increasing the tropospheric extinction by a factor of ~ 1.5 seems to fit the data better at 20°S , however, this could be related to an underestimate of the CH_4 opacity as discussed above. There is a prominent increase in tropospheric opacity around the south pole, at latitudes above 40°S . This had been observed previously as a “hood” in narrowband images [e.g., Roe *et al.*, 2002a]. Using the Huygens/DISR extinction profile, we can calculate that tropospheric extinction at the south pole is enhanced by a factor of ~ 1.5 relative to the Huygens/DISR values. The raw images show that the southern hood was more prominent in 2001 and is now decreasing in opacity.

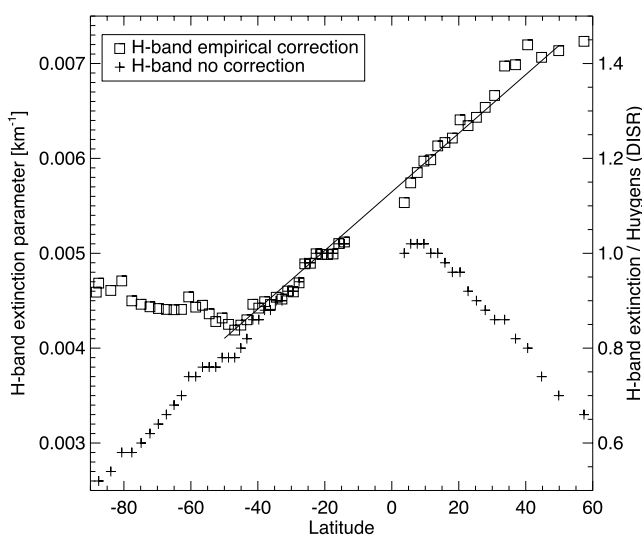


Figure 9. The extinction parameter, k_H , versus latitude at 90°W longitude. Starting at 40°S , the stratospheric extinction increases linearly with latitude into the northern hemisphere. Both the empirically corrected and uncorrected k_H are plotted. Data in the range from 0 to 10°S have been excluded from the fit due to the artifact that is apparent in Figure 8, inset A.

[36] A similar analysis can be performed in H-band, and the southern hood is also measured to be localized at latitudes above 40°S at these wavelengths (Figure 11). Comparison of the enhancement haze relative to extinction

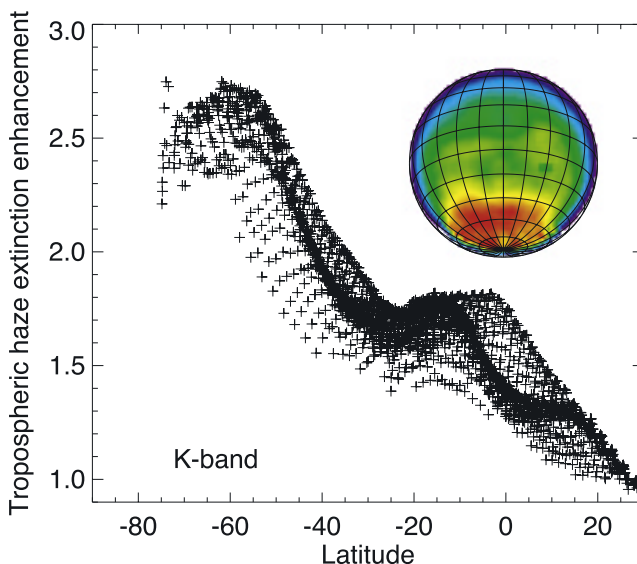


Figure 10. The tropospheric extinction enhancement, measured in K-band (see text for details), is plotted against latitude and shown for each spatial pixel (inset). The south polar hood that is faintly visible in the $2.140\ \mu\text{m}$ image (Figure 2) clearly stands out in the retrieved tropospheric extinction. The peak value for the enhancement near the south pole is a factor of ~ 1.7 greater than at 10°S , the latitude of the Huygens landing site.

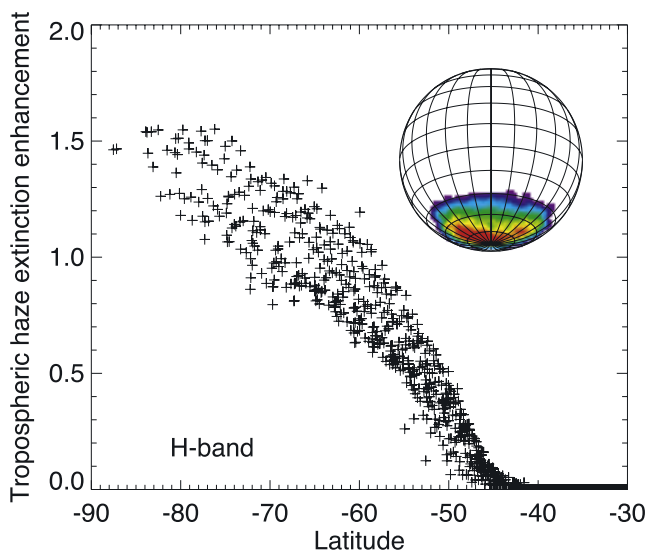


Figure 11. Same as Figure 10, with the tropospheric enhancement fit in H-band. A “hood” is observed around the south pole with an enhancement in tropospheric haze relative to the Huygens/DISR profile [Tomasko *et al.*, 2005]. Note the difference in axes. In H-band the steeper falloff of the calculated I/F (see Figure 7) due to a lack of collisionally induced absorption at this wavelength results in a best fit to the observations when eliminating the tropospheric opacity. An underestimate of the gas-phase opacity likely masks the need for tropospheric aerosol in the retrieval.

at the latitude of the Huygens landing site cannot be made because the best calculated spectrum requires a complete clearing of the troposphere. Once again we interpret the need for this clearing as an underestimate of the gas opacity

in the H-band wavelengths that probe the troposphere. Nonetheless, the relative enhancement in haze from 50°S latitude to the south pole (~ 1.5) is consistent with the K-band measurements.

4.7. Surface Albedo

[37] After both the tropospheric and stratospheric extinction have been fit, the last free parameter in modeling an observed spectrum is the surface albedo. As we described in section 4.4 the surface albedos are fit with the presumption of an underestimate in the gas opacity and the retrieved K-band albedos are overestimated by $\sim 2\%$. We proceed with the assumption that this is a systematic offset and calculate the surface albedos in both H- and K-bands across Titan. Figure 12 shows the retrieved albedos in these bands. The surface albedo variation across the disk matches what we determined qualitatively in section 3 and Figure 3. While the values for the surface albedo are retrieved to be in the same range 6 – 14% for both bands, these values do not include the $\sim 2\%$ overestimate in K-band.

[38] The regions of brightest H-band surface albedo do not correspond to the brightest regions in K-band, and as we discussed above (section 3) both the $5\mu\text{mBS}$ and another analogous bright spot in K-band are located where the H-band albedo is relatively low. Furthermore, it seems that there could be anti-correlation in the brightest H- and K-band regions on Xanadu. The two H-band bright spots directly to the northeast and southwest of the subobserver point are dim regions in the K-band surface albedo map.

5. Conclusion

[39] We have reported simultaneous, multiband, integral-field observations of Titan with SINFONI/VLT and we have used a two-stream radiative transfer model to retrieve the surface albedos, and quantitative enhancements in southern tropospheric and northern stratospheric hazes. The surface

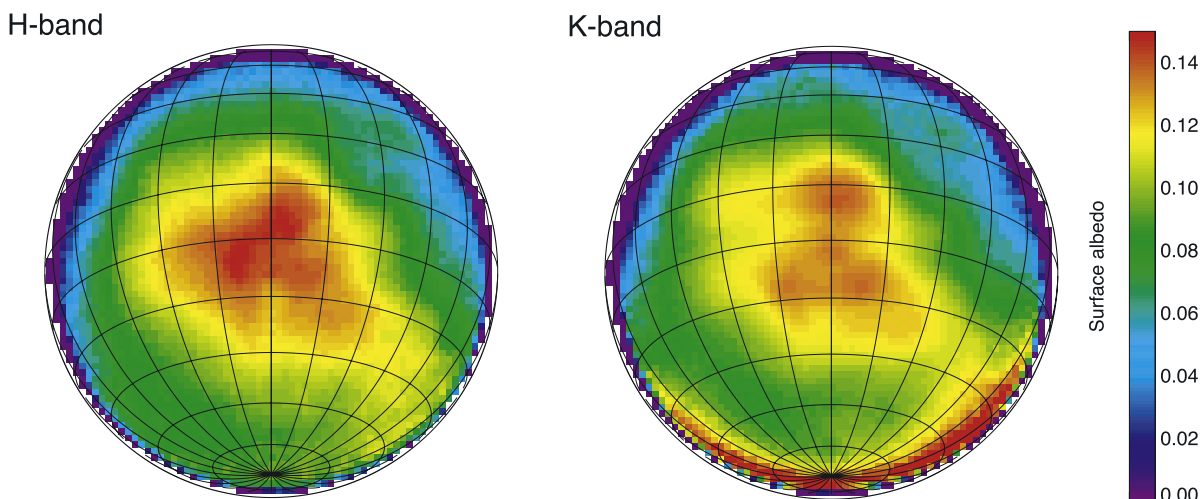


Figure 12. Spectroscopically determined surface albedo maps in H-band and K-band. The measurements at the limb are uncertain due to both the large solar incidence angles at the surface and the uncertainties in the tropospheric haze enhancement retrieval.

albedo maps show that the 2 μm signature of the 5 μmBS is not unique, and in retrospect, the Cassini/VIMS data of Barnes *et al.* [2005] indicates that the 5 μm signature of the 5 μmBS might not be unique either. Both of the bright spots occur on Xanadu, which is known from surface albedo maps to be brighter than other regions of Titan where the 2 μm signature of these bright spots is not seen.

[40] The tropospheric haze enhancement near the south pole is confined to latitudes above 40°S, and aerosol extinction there is retrieved to be enhanced by a factor of ~ 1.7 relative to the latitude of the Huygens landing site. The localization of tropospheric haze has implications for “non-pole-to-pole” circulation and cloud formation [Griffith *et al.*, 2005; Rannou *et al.*, 2006]. The stratospheric extinction is measured to increase linearly at a rate of $0.65 \pm 0.05\%$ per degree latitude from 40°S into the northern midlatitudes. Both of these values have been determined in the context of the Huygens/DISR measurements [Tomasko *et al.*, 2005] that demonstrate a constant tropospheric haze extinction.

[41] The observations presented here reveal that the tropospheric haze enhancement observed in 2001 [Roe *et al.*, 2002a; Ádámkovics *et al.*, 2004], shortly before the summer solstice at the south pole (in October 2002), has thinned and is far less prominent than in 2005. However, the interpretation by Ádámkovics *et al.* [2004] of an enhancement specifically near the altitude of the tropopause must be revised in light of the Huygens/DISR measurements, and further observations are necessary to show if indeed there is a preferential altitude in the troposphere at which the extinction enhancement occurs. The redistribution of tropospheric haze is a new example of large-scale aerosol dynamics, like the seasonal stratospheric haze asymmetry that has been observed, for example, from the Hubble Space Telescope [Lorenz *et al.*, 2004] and from the ground [Gibbard *et al.*, 2004] and modeled by GCM [Rannou *et al.*, 2002].

[42] The altitude sensitivity in our analysis of the observed spectra is limited by the uncertainties in the gas-opacities on the wings of the strong CH₄ bands. Either the weak CH₄ transitions in the HITRAN 2004 database must be assigned and absorption coefficients calculated via line-by-line techniques, or another series of laboratory experiments recording the CH₄ spectrum at a series of temperature and pressures (such as the data used by Irwin *et al.* [2006], only at higher sensitivities) needs to be performed. In addition, there may be new sources of gas-phase opacity at these wavelengths that need to be identified.

[43] Improved gas opacities in these models will facilitate the comparison of H- and K-band surface albedos, and maps of the entire disk will help to determine if there is a relationship between 5 μmBS s and bright continents. Observations of Titan in the J-band (1.0 – 1.3 μm), which are sensitive to smaller particles, may determine if particles of different sizes are redistributed on different timescales.

[44] A simultaneous comparison of multiple transmission bands, or CH₄ “windows,” is one way to constrain the properties of tropospheric aerosol since aerosol scattering and extinction will differ from one band to the next, for a given vertical profile. With the appropriate wavelength and

spatial overlap, such observations will facilitate comparison of Huygens/DISR, Cassini/VIMS, and ground-based measurements.

[45] Along with improving the accuracy of the profile retrieval, this type of analysis will benefit from more frequent observations, so that subtle changes in the aerosol redistribution can be monitored. A long baseline of observations will benefit from the use of integral-field spectroscopy, as it provides the most efficient way to gather the necessary spectra for retrieving the haze distribution. Using SINFONI for such monitoring, as has been done with narrow-band filter imaging (<http://www2.keck.hawaii.edu/science/titan/>), would yield increased vertical resolution via higher spectral resolution, and could discern the detailed motions of haze and clouds.

[46] **Acknowledgments.** We would like to acknowledge the entire SINFONI/SPIFFI team for their observations and for making these data publicly available. We would like to thank Pascal Rannou, Athena Coustenis, and Mathieu Hirtzig for helpful comments on the manuscript. This work was supported in part by NSF grant AST-0205893, NASA grant NNG05GH63G, the UC, Berkeley Center for Integrative Planetary Science grant 8675309, and the Lockheed Martin MIDAS grant.

References

- Ádámkovics, M., I. de Pater, H. G. Roe, S. G. Gibbard, and C. A. Griffith (2004), Spatially-resolved spectroscopy at 1.6 μm of Titan's atmosphere and surface, *Geophys. Res. Lett.*, 31, L17S05, doi:10.1029/2004GL019929.
- Barnes, J. W., et al. (2005), A 5-micron-bright spot on Titan: Evidence for surface diversity, *Science*, 310, 92–95, doi:10.1126/science.1117075.
- Bonnet, H., et al. (2003), Implementation of MACAO for SINFONI at the VLT, in NGS and LGS modes, in *Adaptive Optical System Technologies II*, edited by P. L. Wizinowich and D. Bonaccini, Proc. SPIE Int. Soc. Opt. Eng., 4839, 329–343.
- Bonnet, H., et al. (2004), First light of SINFONI at the VLT, *Messenger*, 117, 17.
- Brown, M. E., A. H. Bouchez, and C. A. Griffith (2002), Direct detection of variable tropospheric clouds near Titan's south pole, *Nature*, 420, 795–797.
- Caldwell, J., et al. (1992), Titan: Evidence for seasonal change—A comparison of Hubble Space Telescope and Voyager images, *Icarus*, 97, 1–9, doi:10.1016/0019-1035(92)90053-A.
- Colina, L., R. C. Bohlin, and F. Castelli (1996), The 0.12–2.5 micron absolute flux distribution of the Sun for comparison with solar analog stars, *Astron. J.*, 112, 307–315, doi:10.1086/118016.
- Eisenhauer, F., et al. (2003a), The universe in 3D: First observations with SPIFFI, the infrared integral field spectrometer for the VLT, *Messenger*, 113, 17–25.
- Eisenhauer, F., et al. (2003b), SINFONI—Integral field spectroscopy at 50 milli-arcsecond resolution with the ESO VLT, in *Instrument Design and Performance for Optical/Infrared Ground-based Telescopes*, edited by M. Iye and A. Moorwood, Proc. SPIE Int. Soc. Opt. Eng., 4841, 1548–1561.
- Fulchignoni, M., et al. (2005), In situ measurements of the physical characteristics of Titan's environment, *Nature*, 438, 785–791, doi:10.1038/nature04314.
- Gibbard, S. G., I. de Pater, B. A. Macintosh, H. G. Roe, C. E. Max, E. F. Young, and C. P. McKay (2004), Titan's 2 μm surface albedo and haze optical depth in 1996–2004, *Geophys. Res. Lett.*, 31, L17S02, doi:10.1029/2004GL019803.
- Griffith, C. A., and T. Owen (1992), Observing the surface of Titan through near-infrared windows in its atmosphere, in *Symposium on Titan*, Eur. Space Agency. Spec. Publ., ESA-SP 338, 199–204.
- Griffith, C. A., T. Owen, and R. Wagener (1991), Titan's surface and troposphere, investigated with ground-based, near-infrared observations, *Icarus*, 93, 362–378.
- Griffith, C. A., T. Owen, G. A. Miller, and T. Geballe (1998), Transient clouds in Titan's lower atmosphere, *Nature*, 395, 575–578.
- Griffith, C. A., T. Owen, T. R. Geballe, J. Rayner, and P. Rannou (2003), Evidence for the exposure of water ice on Titan's surface, *Science*, 300, 628–630, doi:10.1126/science.1081897.
- Griffith, C. A., et al. (2005), The evolution of Titan's mid-latitude clouds, *Science*, 310, 474–477, doi:10.1126/science.1117702.

- Hilico, J. C., M. Loete, and L. R. Brown (1992), Line strengths of the $\nu_2 + \nu_3$ and $\nu_3 - \nu_2$ bands of methane ($^{12}\text{CH}_4$), *J. Mol. Spectrosc.*, *152*, 229–251, doi:10.1016/0022-2852(92)90134-A.
- Hirtzig, M., A. Coustenis, O. Lai, E. Emsellem, A. Pecontal-Rousset, P. Rannou, A. Negrão, and B. Schmitt (2005), Near-infrared study of Titan's resolved disk in spectro-imaging with CFHT/OASIS, *Planet. Space Sci.*, *53*, 535–556, doi:10.1016/j.pss.2004.08.006.
- Hourdin, F., O. Talagrand, R. Sadourmy, R. Courtin, D. Gautier, and C. P. McKay (1995), Numerical simulation of the general circulation of the atmosphere of Titan, *Icarus*, *117*, 358–374.
- Hutzell, W. T., C. P. McKay, and O. B. Toon (1993), Effects of time-varying haze production on Titan's geometric albedo, *Icarus*, *105*, 162–174, doi:10.1006/icar.1993.1116.
- Hutzell, W. T., C. P. McKay, O. B. Toon, and F. Hourdin (1996), Simulations of Titan's brightness by a two-dimensional haze model, *Icarus*, *119*, 112–129, doi:10.1006/icar.1996.0005.
- Irwin, P. G. J., L. A. Sromovsky, E. K. Strong, K. Sihra, N. A. Teanby, N. Bowles, S. B. Calcutt, and J. J. Remedios (2006), Improved near-infrared methane band models and k-distribution parameters from 2000 to 9500 cm^{-1} and implications for interpretation of outer planet spectra, *Icarus*, *181*, 309–319, doi:10.1016/j.icarus.2005.11.003.
- Khare, B. N., C. Sagan, E. T. Arakawa, F. Suits, T. A. Callcott, and M. W. Williams (1984), Optical constants of organic tholins produced in a simulated Titanian atmosphere—From soft X-ray to microwave frequencies, *Icarus*, *60*, 127–137.
- Kouvaris, L. C., and F. M. Flasar (1991), Phase equilibrium of methane and nitrogen at low temperatures—Application to Titan, *Icarus*, *91*, 112–124, doi:10.1016/0019-1035(91)90131-C.
- Lellouch, E., A. Coustenis, D. Gautier, F. Raulin, N. Dubouloz, and C. Frere (1989), Titan's atmosphere and hypothesized ocean—A reanalysis of the Voyager 1 radio-occultation and IRIS 7.7-micron data, *Icarus*, *79*, 328–349.
- Lorenz, R. D., and N. O. Rennó (2002), Work output of planetary atmospheric engines: Dissipation in clouds and rain, *Geophys. Res. Lett.*, *29*(2), 1023, doi:10.1029/2001GL013771.
- Lorenz, R. D., E. F. Young, and M. T. Lemmon (2001), Titan's smile and collar: HST observations of seasonal change 1994–2000, *Geophys. Res. Lett.*, *28*, 4453–4456.
- Lorenz, R. D., P. H. Smith, and M. T. Lemmon (2004), Seasonal change in Titan's haze 1992–2002 from Hubble Space Telescope observations, *Geophys. Res. Lett.*, *31*, L10702, doi:10.1029/2004GL019864.
- Margolis, J. S. (1988), Measured line positions and strengths of methane between 5500 and 6180 cm^{-1} , *Appl. Opt.*, *27*, 4038–4051.
- McKay, C. P., J. B. Pollack, and R. Courtin (1989), The thermal structure of Titan's atmosphere, *Icarus*, *80*, 23–53.
- McKay, C. P., A. Coustenis, R. E. Samuelson, M. T. Lemmon, R. D. Lorenz, M. Cabane, P. Rannou, and P. Drossart (2001), Physical properties of the organic aerosols and clouds on Titan, *Planet. Space Sci.*, *49*, 79–99.
- McKellar, A. R. W. (1989), Low-temperature infrared absorption of gaseous N_2 and $\text{N}_2 + \text{H}_2$ in the 2.0–2.5 micron region—Application to the atmospheres of Titan and Triton, *Icarus*, *80*, 361–369, doi:10.1016/0019-1035(89)90146-2.
- Niemann, H. B., et al. (2005), The abundances of constituents of Titan's atmosphere from the GCMS instrument on the Huygens probe, *Nature*, *438*, 779–784, doi:10.1038/nature04122.
- Porco, C. C., et al. (2005), Imaging of Titan from the Cassini spacecraft, *Nature*, *434*, 159–168.
- Rank, D. H., D. P. Eastman, G. Skorinko, and T. A. Wiggins (1961), Fine structure in the lines of the $2\nu_3$ band of methane, *J. Mol. Spectrosc.*, *5*, 78–82, doi:10.1016/0022-2852(61)90069-8.
- Rannou, P., F. Hourdin, and C. P. McKay (2002), A wind origin for Titan's haze structure, *Nature*, *418*, 853–856.
- Rannou, P., F. Hourdin, C. P. McKay, and D. Luz (2004), A coupled dynamics-microphysics model of Titan's atmosphere, *Icarus*, *170*, 443–462, doi:10.1016/j.icarus.2004.03.007.
- Rannou, P., F. Montmessin, F. Hourdin, and S. Lebonnois (2006), The latitudinal distribution of clouds on Titan, *Science*, *311*, 201–205, doi:10.1126/science.1118424.
- Roe, H. G., I. de Pater, B. A. Macintosh, S. G. Gibbard, C. E. Max, and C. P. McKay (2002a), Note: Titan's atmosphere in late southern spring observed with adaptive optics on the W. M. Keck II 10-meter telescope, *Icarus*, *157*, 254–258.
- Roe, H. G., I. de Pater, B. A. Macintosh, and C. P. McKay (2002b), Titan's clouds from Gemini and Keck adaptive optics imaging, *Astrophys. J.*, *581*, 1399–1406.
- Roe, H. G., A. H. Bouchez, C. A. Trujillo, E. L. Schaller, and M. E. Brown (2005a), Discovery of temperate latitude clouds on Titan, *Astrophys. J. Lett.*, *618*, L49–L52, doi:10.1086/427499.
- Roe, H. G., M. E. Brown, E. L. Schaller, A. H. Bouchez, and C. A. Trujillo (2005b), Geographic control of Titan's mid-latitude clouds, *Science*, *310*, 477–479, doi:10.1126/science.1116760.
- Rothman, L. S., et al. (2005), The HITRAN 2004 molecular spectroscopic database, *J. Quant. Spectrosc. Radiat. Transfer.*, *96*, 139–204.
- Samuelson, R. E., and L. A. Mayo (2001), Thermal infrared properties of Titan's stratospheric aerosol, *Icarus*, *91*, 207–219.
- Tokano, T., F. M. Neubauer, M. Laube, and C. P. McKay (2001), Three-dimensional modeling of the tropospheric methane cycle on Titan, *Icarus*, *153*, 130–147, doi:10.1006/icar.2001.6659.
- Tomasko, M. G., et al. (2005), Rain, winds and haze during the Huygens probe's descent to Titan's surface, *Nature*, *438*, 765–778, doi:10.1038/nature04126.
- Toon, O. B., C. P. McKay, R. Courtin, and T. P. Ackerman (1988), Methane rain on Titan, *Icarus*, *75*, 255–284, doi:10.1016/0019-1035(88)90005-X, 1988.
- Toon, O. B., C. P. McKay, T. P. Ackerman, and K. Santhanam (1989), Rapid calculation of radiative heating rates and photodissociation rates in inhomogeneous multiple scattering atmospheres, *J. Geophys. Res.*, *94*, 16,287–16,301.
- Toon, O. B., C. P. McKay, C. A. Griffith, and R. P. Turco (1992), A physical model of Titan's aerosols, *Icarus*, *95*, 24–53.
- Tran, T. T., and P. Rannou (2004), Comparing 3D spherical Monte-Carlo and 2-stream parallel plane simulation of far-field backscattering image of Titan, *Notes Pôle Planétol. Inst. Pierre Simon Laplace*, *2*, pp. 18–38, Gif sur Yvette, France.
- West, R. A., H. Hart, K. E. Simmons, C. W. Hord, L. W. Esposito, A. L. Lane, R. B. Pomphrey, D. L. Coffeen, and M. Sato (1983), Voyager 2 photopolarimeter observations of Titan, *J. Geophys. Res.*, *88*, 8699–8708.
- Young, E. F., P. Rannou, C. P. McKay, C. A. Griffith, and K. Noll (2002), A three-dimensional map of Titan's tropospheric haze distribution based on Hubble Space Telescope imaging, *Astron. J.*, *123*, 3473–3486.

M. Ádámkovics and I. de Pater, Department of Astronomy, University of California, 601 Campbell Hall, Berkeley, CA 94720, USA. (mate@berkeley.edu)

F. Eisenhauer and R. Genzel, Max-Planck-Institut für extraterrestrische Physik (MPE), Giessenbachstrasse, Postfach 1312, D-85741 Garching, Germany.

C. A. Griffith, Lunar and Planetary Laboratory, University of Arizona, Tucson, AZ 85721, USA.

M. Hartung, European Southern Observatory, Alonso de Cordova 3107, Santiago 19, Chile.